Dalton Transactions

Systematic study of the synthesis and coordination of 2-(1,2,3-triazol-4-yl)-pyridine to Fe(II), Ni(II) and Zn(II); ion-induced folding into helicates, mesocates and larger architectures, and application to magnetism and self-selection

Journal:	*Dalton Transactions*
Manuscript ID:	DT-ART-01-2015-000233.R2
Article Type:	Paper
Date Submitted by the Author:	01-Jul-2015

Complete List of Authors:	Wu, Nan; Queen's University, Chemistry Melan, Caroline; Université d'Angers, Chimie Stevenson, Kristina; Queen's University, Chemistry Fleischel, Olivier; BASF, Guo, Huan; Queen's University, Chemistry Habib, Fatemah; University of Ottawa, Chemistry Holmberg, Rebecca; University of Ottawa, Chemistry Murugesu, Muralee; University of Ottawa, Chemistry Mosey, Nicholas; Queens University, Department of Chemistry Nierengarten, Hélène; niversité de Strasbourg, Chimie Petitjean, Anne; Queens University, Chemistry

TOC

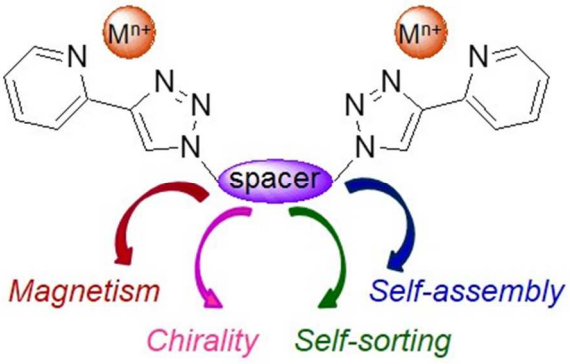

Despite its apparent similarity to 2,2'-bipyridine, the 2-pyridyl-1,2,3-triazole chelate displays unique coordination properties. Within bifunctional ligands, its weaker nature allows the expression of subtle effects, such as the nature of the spacer, on a variety of physical properties.

Cite this: DOI: 10.1039/c0xx00000x

www.rsc.org/xxxxxx

Full paper

Systematic study of the synthesis and coordination of 2-(1,2,3-triazol-4-yl)-pyridine to Fe(II), Ni(II) and Zn(II); ion-induced folding into helicates, mesocates and larger architectures, and application to magnetism and self-selection

Nan Wu,[a] Caroline F. C. Melan,[b] Kristina A. Stevenson,[a] Olivier Fleischel,[c] Huan Guo,[a] Fatemah Habib,[d] Rebecca J. Holmberg,[d] Muralee Murugesu[d], Nicholas J. Mosey,[a] Hélène Nierengarten,[e] and Anne Petitjean*[a]

Received (in XXX, XXX) Xth XXXXXXXXX 20XX, Accepted Xth XXXXXXXXX 20XX
DOI: 10.1039/b000000x

With its facile synthesis, the pyridine-1,2,3-triazole chelate is an attractive building block for coordination-driven self-assembly. When two such chelates are bridged by a spacer and exposed to cations of octahedral geometrical preference, they generally self-assemble in dinuclear triple-stranded structures in the solid state and in solution in the presence of non-coordinating counter-ions. In solution, a wider range of architectures may nevertheless form, depending on the nature of the spacer. A systematic study of the spacer and substitution pattern is therefore presented, which allows assessing the various factors affecting self-assembly around the pyridine-1,2,3-triazole chelate, as well as the stereochemical control in these architectures. Applications to chirality, magnetism and system selection are discussed, and involve Fe(II), Ni(II), Zn(II) and Cu(I) cations.

Introduction

The copper-catalyzed azide-alkyne cycloaddition (CuAAC) reaction has received tremendous attention and found many applications thanks to its high efficiency and ease of purification, functional group tolerance and compatibility with various solvents including water.[1] Recently, the resulting nitrogen-rich 1,2,3-triazole has also been recognized in supramolecular chemistry as a folding codon[2] and a ligand for metal ions.[3-4] New coordination motifs based on this unit display unique luminescence,[3c,4e] magnetism[4f] and electrochemistry.[4b,d-e] Multinuclear 1,2,3-triazole-based self-assembled architectures such as cages are emerging.[4c,h] Surprisingly, helicates,[5] which are among the most popular self-assembled structures due to their unique properties (*e.g.*, chirality, energy transfer)[5] have barely been explored in the 1,2,3-triazole series,[4g,6] despite the attractive features of the nitrogen-rich triazole unit (*e.g.*, multiple interaction modes, limited steric hindrance, moderate ligand field). However, as with most multinuclear self-assembled architectures, the role of the spacer bridging two coordination units, as well as the substitution state of the ligands, are critical in determining the folding outcome.[7] We report herein a systematic study of the self-assembly of dinuclear architectures based on the 1,2,3-triazolylpyridine chelate, by varying the flexibility and length of the spacer (**L1**-**L6**, Scheme 1), and changing the substitution pattern of the terminal pyridine (**L1M**, **L3M** and **L4M**, Scheme 1), giving insights into the impact on stereochemical, thermodynamic and magnetic properties.

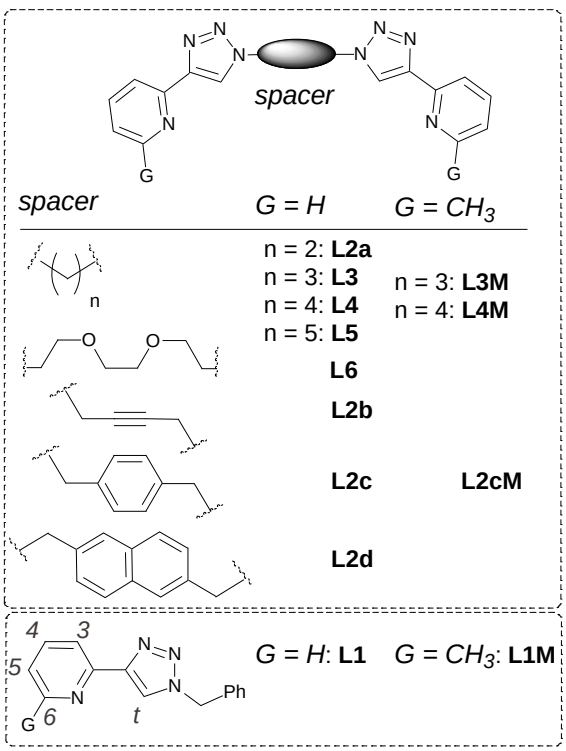

Scheme 1 Monofunctional (**L1**,[3b,4a,b,e,6] **L1M**) and bifunctional (**L2a**, **L2b**, **L2c**,[4b] **L2d**,[4g] **L3**,[4a,6] **L4**, **L5** and **L6**) ligands used. The numbering on the mono-chelating unit (bottom) relates to NMR assignments.

Synthesis of ligands and complexes

One of the strengths of the triazole unit is its facile and efficient synthesis starting from organic azide using copper catalysed alkyne azide cycloaddition.[1] In an effort to avoid isolating the potentially explosive organic azides, their *in-situ* preparation was achieved from alkylbromides through an S_N2 reaction with sodium azide. As described by Crowley's group,[4a] both the S_N2 and CuAAC reactions may be carried out in a one pot reaction, by mixing all reagents in a combination of organic solvent (*e. g*., DMF or *t*BuOH) and water. In our hands, this method works very efficiently for electrophiles that are activated through the proximity of π systems, as in propargylic and benzylic/benzylic-like positions (*e.g.*, **L2b**, **L2c**, **L2d**), or through inductive effects of the second bromide, as in **L2a**. However, yields are moderate for non-activated alkyl bromides (*e. g*., organic halides where the two leaving groups are separated by more than two methylene units). In order to promote a complete S_N2 reaction on these electrophiles, it is beneficial to split this one pot conversion into two processes: the S_N2 reaction first efficiently takes place in the absence of any protic solvent (*e. g*., in pure DMF) to complete the *in-situ* synthesis of the organic azide, after which the CuAAC reagents and water are added to transform the organic azide into the triazole ring. The overall conversion is therefore efficiently accomplished in a one pot, although through two consecutive processes. In some cases, heating was applied after the first reaction and before addition of the CuAAC reagents in order to ensure full S_N2 conversion.

The nickel(II) and iron(II) complexes were either generated *in situ* on a small scale for direct ^{1}H NMR analysis, and isolated by crystallization (when amenable) of an acetonitrile solution through slow diffusion of diethylether (74-95% recovery yields). Complexes that failed to produce crystals were isolated by concentrating the acetonitrile solution to dryness, followed by hot digestion with dichloromethane to remove any unbound ligand (51-55% recovery yield). Complexes of **L3** with iron(II) were prepared in degassed solvents and crystallized under argon to ensure no iron(III) would be responsible for the observed magnetic behaviour (*vide infra*). Iron(II) complexes with the other ligands were consistent with Fe(II) redox state and were not observed to be air sensitive. They therefore can be handled in air.

Self-assembly of dinuclear complexes

Self-assembly in the solid state

With two chelating groups connected through a semi-rigid spacer, ligand **L2c** is designed to form dinuclear multistranded complexes akin to those derived from 2,2'-bipyridines.[5b] Coordination of **L2c** to Fe^{II} and Ni^{II} indeed results in isostructural helicates, with two pseudo-octahedral coordination centers of identical chirality (Λ, Fig. 1a) bridged by a central *p*-xylyl fragment of opposite twist.[4g] As anticipated, the Fe-N bond lengths in $Fe(\mathbf{L1})_3^{4+}$ and $Fe_2(\mathbf{L2c})_3^{4+}$ are nearly identical, and typical of low-spin iron(II).[6a] Similar properties are found in the solid-state structure of the naphthalene $[Fe_2(\mathbf{L2d})_3](BF_4)_2$ analog.[4g] Despite all efforts, attempts to produce single crystals from complexes derived from ethylene-like spacers **L2a** and **L2b** have been unsuccessful. However, increasing the number of CH_2 units, the Fe^{II} and Ni^{II} complexes of the propylene-derived **L3** ligand are found to also be isostructural in the solid-state and result in mesocates due to the chirality reversal induced by the propylene spacer (Fig. 1b). In our hands, longer ligands (**L4-L6**) have not been amenable to single crystal formation with either iron(II) or nickel(II).

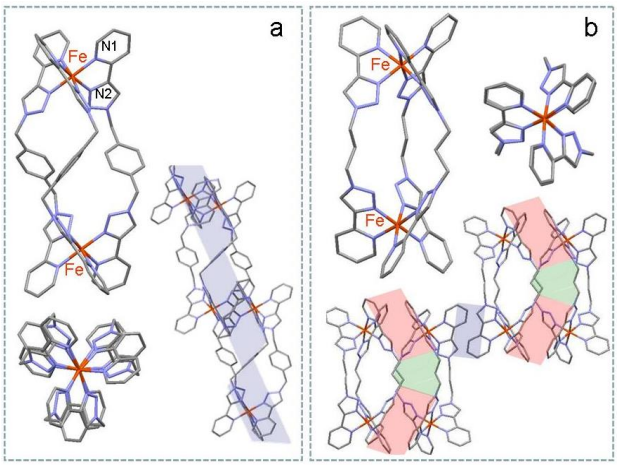

Fig. 1 Side and top views of the dinuclear a) $Fe_2(\mathbf{L2c})_3^{4+}$ (only one enantiomer shown) and b) $Fe_2(\mathbf{L3})_3^{4+}$ at 77 K. Solid-state self-assembly is also illustrated (blue boxes : head-to-tail pyridine-triazole dimers; pink boxes: head-to-head pyridine-triazole dimers, green shade: van der Waals contacts).[4g] Anions and solvents are omitted for clarity. Selected distances (Å): a) Fe-N2: 1.939(2), Fe-N1: 1.998(2); Fe···Fe: 11.391; b) Fe-$N_{triazole}$: 1.925-1.945, Fe-$N_{pyridine}$: 1.995-2.012, Fe···Fe: 9.878.

Based on the crystal structures above illustrating the stereochemical effect of even-numbered and odd-numbered spacers (**L2c** and **L3**, respectively), the helicate *vs* mesocate selection rules defined for 2,2'-bipyridyl- and catechol-based systems[5b] may be at work here as well. In these two families of ligands, the zigzag conformational preference of alkyl fragments has been proposed to favour mesocates for spacers with an odd number of carbon atoms, and helicates for spacers with an even number of carbon atoms (here, a *p*-xylyl unit acts as an extended CH_2-CH_2 bridge). However, the limited crystallographic data and possible bias introduced by packing forces in the solid state invite more in-depth exploration of self-assembly through solution studies.

Self-assembly in solution: influence of the spacer length analysed by NMR and UV-vis spectroscopies.

Stoichiometry as well as relative binding strength in both iron(II) and nickel(II) families were first explored by UV-vis absorption titrations. Diamagnetic iron(II) species were then studied by ^{1}H NMR spectroscopy in search for structural information.

Comparing complexes derived from the aliphatic spacers (from ethylene, **L2a**, to pentylene, **L5**), saturated 3:2 ligand/cation species were exclusively formed in the 10^{-5} M range for both nickel(II) and iron(II) with tetrafluoroborate counterions, as evidenced by the plateau observed at around 0.7 ion/ligand ratio, in the absorbance profile at 305 nm and 425 nm respectively (Fig. 2). A closer look at the absorbance profiles indicates that all ligands form very tight complexes with iron(II), as the absorbances show a plateau starting at a 0.67 ratio for all ligands (Fig. 2b). The iron complexes are so tight that UV-vis titrations at these concentrations fail to provide quantitative distinction between the relative association constants. However, the nickel

titration profiles show a differentiation between very tight binding for **L3** and **L4** (sharp transition at the 0.67 ratio, Fig. 2a), and strong binding for **L2a** and **L5** (smoother transition, saturating at a higher ratio, Fig. 2a). The propylene and butylene spacers therefore accommodate the triple stranded assembly best. On the contrary, the shorter ethylene spacer (**L2a**) may induce increased strain and/or electrostatic repulsion (this aspect will be discussed further below). Furthermore, the longer pentylene spacer with increased degrees of freedom may be entropically more disfavoured.

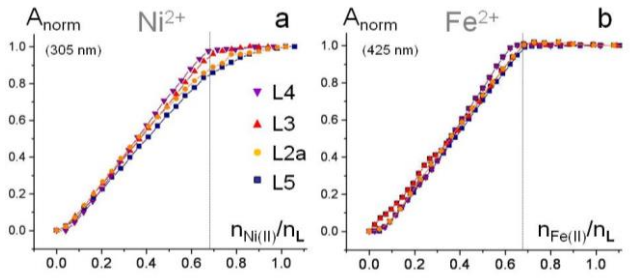

Fig. 2 Overlay of UV-vis titration profiles of a) nickel(II) and b) iron(II) complexes of **L2a**, **L3**, **L4** and **L5** (CH_3CN, 25 °C).

^{1}H NMR analysis allows to better understand the triple-stranded structures of the iron(II) complexes for all ligands (Fig. 3).

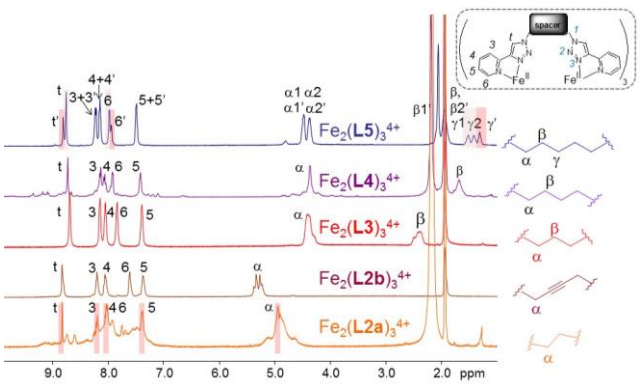

Fig. 3 Comparative ^{1}H NMR of $[Fe_2(\mathbf{L})_3](BF_4)_4$ complexes with L = **L2a**, **L2b**, **L3**, **L4** and **L5** (CD_3CN, 25 °C, c~10 mM). The complex with **L3** was freshly prepared (3:2 **L3**/Fe^{2+} mixture). Top: H numbering in black, triazole nitrogen numbering in blue.

As seen in Fig. 3, the short spacer in **L2a** leads to a mixture of species among which sharp peaks correspond to the well-defined $Fe_2(\mathbf{L2a})_3^{4+}$ triple-stranded complex, as evidenced by the typical relative chemical shifts of the H3 and H6 pyridyl protons (see above) which are easily extracted through COSY analysis (ESI†). The broader signals likely result from coexisting oligomers (*vide infra*). When the two carbon atoms of the spacer are spread further apart, for instance with an ethynyl (**L2b**, Fig. 3), a phenyl (**L2c**, ESI†) or a naphthyl group (**L2d**, ESI†), only one well-defined species is observed. The short ethylene spacer in **L2a** is further discussed below. With a propylene spacer which is one carbon atom longer, ligand **L3** mixed with $[Fe(H_2O)_6](BF_4)_2$ in a 3:2 ratio only leads to one well-defined species. Surprisingly, the butylene spacer of **L4** not only forms a major triple-stranded structure, but also minor side-products (see small peaks in Fig. 3). The same minor side-products are observed irrespective of the preparation method, *i.e.* fresh 3:2 **L4**/Fe^{2+} mixture or isolation of the iron complexes. These side-products are likely coexisting larger architectures (*vide infra*). Interestingly, the pentylene spacer shows well-defined signals consistent with two species only (shaded differently in Fig. 3). Both species correspond to triple-stranded dinuclear complexes similar to the other $Fe_2(\mathbf{L})_3^{4+}$ complexes. Significantly different signatures appear in the aliphatic region, and in particular in the signals of the γ protons (Fig. 3). As observed in other chelating systems,[5b] the central CH_2 group is essential in differentiating various triple-stranded structures. In the 'primed species' (Fig. 3), the γ protons experience an identical environment which is characteristic of a helicate species (each proton faces the 'nitrogen' end of one chelate unit and the CH edge of the other, Fig. 4a).[5,9a] The γ protons of the 'non-primed species' show a diastereotopic signature signifying that they perceive a different environment, and therefore belong to a mesocate structure (the H(2) proton in Fig. 4b faces the 'nitrogen' ends of both chelates, whereas H(1) in Fig. 4b faces the two CH edges of the chelates).

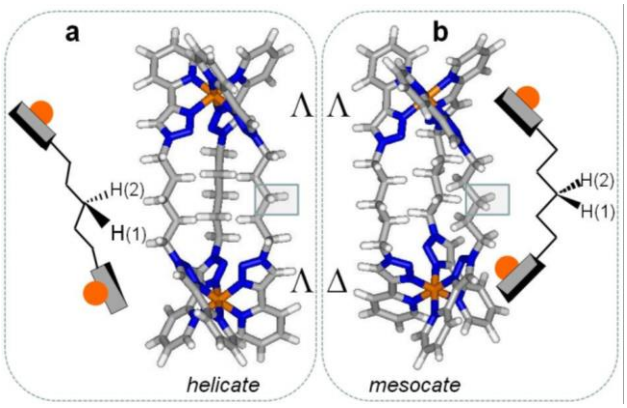

Fig. 4 Cartoon representation of the environments experienced by the central methylene protons of odd-numbered alkyl spacers in a) helicate and in b) mesocate. Rough models of $Fe_2(\mathbf{L5})_3^{4+}$ helicate (a) and mesocate (b) are also represented. The central methylene group is circled in grey and specified on the cartoons.

Based on the above assignment rationale, the ratio of helicate to mesocate for $Fe_2(\mathbf{L5})_3^{4+}$ is 1:2 as determined by the intensities of the ^{1}H NMR signals. The preference for the mesocate structure agrees with the odd/even rule which has been rationalized based on the preferential zigzag conformational preference of alkyl spacers.[5b] However, with the pyridyl-triazole chelates, rough molecular models indicate that only a very small deviation from an 'all-staggered' conformation allows access to the helicate architecture (Fig. 4a), which supports a significant population of the helicate structure. Indeed, as the alkyl spacer length increases, a smaller helical twist in the spacer region is required to form the helicate structure. As a result, a minute energy difference in the conformational energy profile is expected between the helicate and mesocate, leading to coexisting species. In the present study focusing on pyridyl-1,2,3-triazole chelates, the transition to helicate+mesocate mixture starts with the pentylene spacer. More generally speaking, this transition point will vary from one system to the next, depending on several parameters influencing flexibility. The odd/even number of carbons within the linker itself is one parameter, as stressed by other investigators.[5]Another one is the orientation of the first bond emerging from the chelating unit, and leading to the linker, relative to a virtual line

defined by the two donor atoms in the chelate. Here, the $(N1)_{triazole}$-Cα bond and the $N_{Pyridine}$-$(N3)_{triazole}$ line (Fig. 3) are not quite parallel. However, this system is probably mechanically closer to a 5,5'-substituted-2,2'-bipyridyl-type system than to a 4,4'-substituted-2,2'-bipyridyl architecture, the latter suffering from greater steric limitations. These various bond orientations impact the flexibility of the linker to various degrees, and thereby impact the accessibility of helicate *vs* mesocate structures. Finally, the actual chemical nature of the 'connection point' between the chelating unit and the start of the linker plays a significant role in tuning the odd/even number rule; its own conformational energy profile dictates conformational restrictions which can tune the number of carbon atoms at which both helicate and mesocate start coexisting. In the present example, a simple, minimal twist of the 'bottom' Cα-$(N1)_{triazole}$ bond to the right (Fig. 4a) or to the left (Fig. 4b) inverts the chirality of the 2nd (bottom) metal center, so the transition point to a helicate+mesocate mixture starts as early as in the pentylene spacer. Rich examples involving an amide connection point to 2-2'-bipyridine[9b] and hydroxypyridine[9c] chelates harness the weak interactions offered by the amide unit (with solvents) to restrict the available conformations and control the helicate/mesocate outcome. With catechol chelating units, conformational restrictions can be imposed by the 'inner' catechol oxygens binding to cationic guest at the corners of the cavity, resulting in the selection of helical *vs* side-by-side architectures.[5c] Overall, in the pyridyl-triazole family connected by alkyl spacers, the present comparison therefore highlights that (i) the odd-even rule only holds up to the length of a butylene spacer, and (ii) the even numbered spacers (**L2**, **L4**) induces oligomer formation at mM concentrations (Fig. 3), whereas the odd-numbered spacers only favour folding into well-defined species.

As reported above, the ethylene spacer in **L2a** stands out: it leads to less stable complexes at sub-micromolar concentrations (UV-vis, Fig. 2) and to a significant amount of oligomers at millimolar concentrations (^{1}H NMR, Fig. 3). The more limited stability of a $Fe_2(\mathbf{L2a})_3^{4+}$ triple-stranded complex may stem from one or both of the following effects: (i) the closer proximity of the two divalent Fe^{2+} centers resulting in increased mutual electrostatic repulsion, and/or (ii) the proximity of all six 1,2,3-triazolyl N2 nitrogen atoms, and consequent lone pair electronic repulsion near the center of the triple-stranded structure (Fig. 1 gives an idea of the distribution of the three N2 ('middle') nitrogen atoms within triple-stranded helicates and mesocates, yet in a context where both coordination units are fairly far apart). In order to assess the relative contribution of those two effects to the limited stability of $Fe_2(\mathbf{L2a})_3^{4+}$, a comparative study of the Zn^{2+} complexes with two '**L2**-type' ligands was undertaken. The diamagnetic nature of Zn^{2+} complex facilitates structural and stability studies through ^{1}H NMR titrations. Ligands **L2a** and **L2c**, with ethylene and *p*-xylyl spacers respectively, offer similar rigidity but a significant difference in ion-ion distances (the $Fe^{2+}\cdots Fe^{2+}$ distance is 11.4 Å in the X-ray structure of $[Fe_2(\mathbf{L2c})_3](BF_4)_4$, and ~7.7 Å in a rough model of $Fe_2(\mathbf{L2a})_3^{4+}$). By ^{1}H NMR, the *p*-xylyl-based **L2c** shows the gradual formation of a triple-stranded structure first, from 0.1 to 0.7 equivalent of Zn^{2+} (Fig. 5b, bottom part; note the shielding of the pyridyl proton H6 and diastereotopic protons in the CH_2 group, which are typical of a triple-stranded assembly), followed by dissociation into a double-stranded species from 0.8 equivalents and on (Fig. 5b, top). The signature of the double-stranded structure warrants a few comments. Contrary to the structure at 0.7 equivalent of Zn^{2+}, the methylene groups are not diastereotopic anymore (on the NMR time-scale). Importantly, the pyridyl proton H6 appears at high chemical shift, consistent with coordination outside of the shielding cone of neighbouring aromatic ligands. The protons of the phenyl ring ('a') however, undergo significant shielding, possibly due to a side-by-side arrangement.

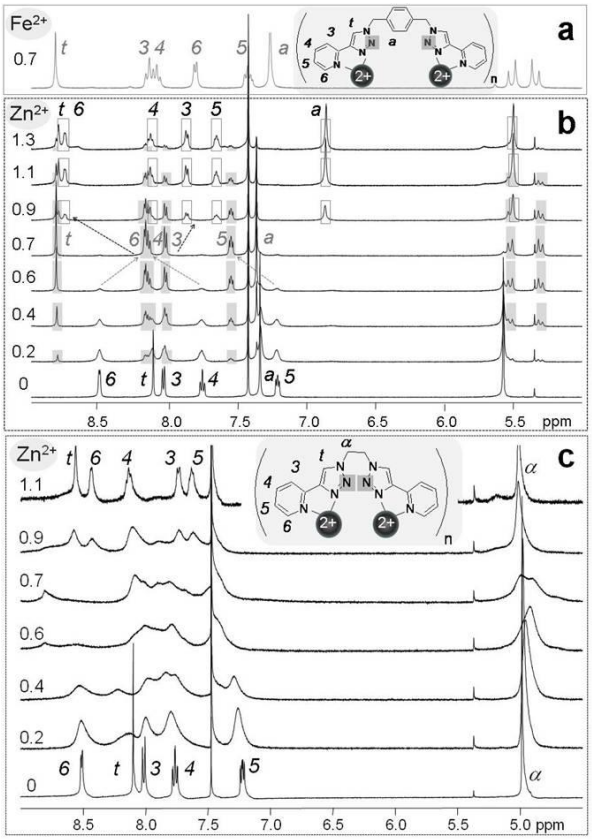

Fig. 5 a) ^{1}H NMR spectrum of $Fe_2(\mathbf{L2c})_3^{4+}$, prepared **L2c** with 0.7 equivalent of Fe^{2+} in CD_3CN, given for reference. b) Titration of $Zn(OTf)_2$ to a solution of **L2c** (5:3 $CDCl_3/CD_3CN$, 25 °C, 500 MHz, $[\mathbf{L2c}]_0$ = 10 mM); grey shading signals the triple-stranded $Zn_2(\mathbf{L2c})_3^{4+}$ complex; black rectangles highlight the 1:1 double-stranded $Zn_2(\mathbf{L2c})_2^{4+}$ species. c) Titration of $Zn(OTf)_2$ to a solution of **L2a** (1:1 $CDCl_3/CD_3CN$, 25 °C ,400 MHz, $[\mathbf{L2a}]_0$ = 14 mM). The numbers below the metal ion on the left correspond to number of equivalents of M^{2+} with regards to the ligand. The triazole N2 nitrogen atom is shaded in grey on the chemical structures of the complexes.

By comparison with the *p*-xylyl spacer, the ethylene spacer is characterized by broad signals all along the titration (0.2-0.9 equivalent of Zn^{2+}), and only leads to reasonably well-defined signals after 1.0 equivalent. The species formed at 1.0 equivalent is, in all likelihood, the double-stranded $[Zn_2(\mathbf{L2a})_2]^{4+}$ complex: the chemical shifts and ordering of the aromatic protons are similar to that in $[Zn_2(\mathbf{L2c})_2]^{4+}$. In addition, water gets involved in binding after 0.8 equivalents in both cases (moving exchangeable water peak not shown), which confirms the availability of binding sites on Zn^{2+} in the 0.2-0.8 equiv. range. In both cases, this likely 2:2 species slowly precipitates

quantitatively, as anticipated with the formation of a neutral complex in a relatively polar solvent (two chelates and two triflates around each divalent cation center). The broadening at 1.0 equivalent and above is, however, very limited compared to the very broad patterns observed for **L2a** between 0.2 and 0.8 Zn^{2+} equivalent, suggestive of either polymeric material or intermediate exchange rates, which would be strikingly different from the slow exchange observed with **L2c**.‡ It therefore appears that **L2a** readily forms the $Zn_2(\mathbf{L2a})_2^{4+}$ double-stranded complex at 1.0 equivalent of zinc(II), but fails to form a well-defined triple-stranded complex at 0.7 equivalent. Since both the double- and triple-stranded species would be characterized by a very similar M^{2+}–M^{2+} distance, the electrostatic repulsion between the two divalent metal ions in **L2a**-derived complexes is not expected to be very different. As a result, the main driving force behind the limited stability of the saturated, triple-stranded $[Zn_2(\mathbf{L2a})_3]^{4+}$ complex is very likely a result of the repulsion of the six converging lone pairs of the 'middle' N2 triazole nitrogen atoms (shaded in grey in Fig. 5c). In a double-stranded structure, however, the possibility of organizing the two pyridyl-triazole chelates in a perpendicular arrangement (as in a tetrahedral complex) relieves the lone pair repulsion, leading to efficient double-stranded self-assembly.

The dominant impact of the repulsion between N2 triazole lone pairs over the electrostatic repulsion between the two divalent ions in the pyridyl-triazole system may be analysed by comparison to other chelate families. In the 4,4'-substituted-2,2'-bipyridyl system, a dinuclear iron(II) complex with ligands bearing a short ethylene spacer has been reported with an $Fe^{2+}\cdots Fe^{2+}$ distance of 7.65 Å in the crystalline state,[10] which is very similar to what **L2a** would produce according to a rough model. Although neither yields nor ^{1}H NMR data were provided for the 4,4'-substituted-2,2'-bipyridyl system,[10] it is assumed that the complex was well-defined as determined by TLC and electrochemical analysis. Similarly, in catechol systems, multivalent cations are held at a close distance, as the ethylene spacer is tolerated in a dinuclear triple-strand format,[5] and extra monovalent cations are present in the center of the architecture. However the compensating anionic nature of the strand renders the comparison difficult. Overall, in the present case, two divalent cations seem to be easily accommodated at ~7 Å distance apart, but the close, enforced proximity of the N2 triazole nitrogen lone pairs is more detrimental to the stability of the triple-stranded structure. Assemblies with the **L2a** ligand in the gas phase are discussed further below.

At the other extreme of the spacer length spectrum to **L2a**, a ligand with a very long and flexible spacer composed of three consecutive ethylene-oxide units (**L6**, scheme 1 and Fig. 6) was also prepared and its coordination properties to iron(II), nickel(II) and zinc(II) were explored. UV-vis titration of iron(II) into a solution of **L6** (Fig. 6 top) shows the formation of two consecutive complexes. Up to 0.7 equivalent of iron(II), a first MLCT band at 420 nm corresponds to a 2:3 Fe^{2+}/**L6** complex (Job plot in ESI†). From 0.7 equivalent to 1.0 equivalent of iron(II), a second complex emerges, with an MLCT band growing at 378 nm, corresponding in all likelihood to a 1:1 complex (a Job plot at 373 nm indicates a mixture of 2:3 and 1:1 complexes overall, ESI†). Because of the inherent flexibility of the spacer in the **L6** ligand, its wrapping into a 1:1 complex is expected to occur. However, earlier in the titration, the presence of a 2:3 complex could correspond to a number of folded architectures, including triple-stranded structures. In order to gain insight into this architecture, structural information was sought by ^{1}H NMR. The titration reported in Fig. 6 indicates two regimes: up to 0.7 equivalent, the ligand signals correspond two coexisting ligand forms. One shows two different pyridyl-triazole environments at the beginning of the titration (blue and purple, Fig. 6). The 'purple' set of signals resembles that of the free ligand and initially has the same signal intensities as the 'blue' signals, suggesting that they correspond to the same dissymmetrical, half-bound ligand. These two different chelate units merge into a symmetrical ligand (blue) when more iron(II) is added. The other ligand form (in green) shows bound chelates resembling the previously characterized octahedral iron complexes all along the titration. The cartoon at the bottom right of Fig. 6 offers an explanation to these various spin environments. At the beginning of the titration, the excess ligand surrounds the metal ion by wrapping (symmetrical species, in green in Fig. 6) and partial binding (blue part of the unsymmetrical ligand, Fig. 6). At 0.7 equiv. of iron(II), the spectrum simplifies, with two distinct symmetrical ligands in a 1:2 ratio, both of them fully bound to the iron(II) center (as per the chemical shifts of the triazole *t* and pyridyl proton H6). A likely schematic structure for this ratio is represented in Fig. 6, right, where each of the two iron(II) centers carries a wrapped ligand (in green) and is bridged to the second ion through a third linear ligand (blue, Fig. 6). The latter structure is likely to be the 3:2 ligand/iron(II) complex observed in the UV-vis titration (Fig. 6 top). Hence, the 3:2 ligand/iron(II) complex with a flexible ligand such as **L6** is not a triple-stranded structure of the helicate/mesocate family.

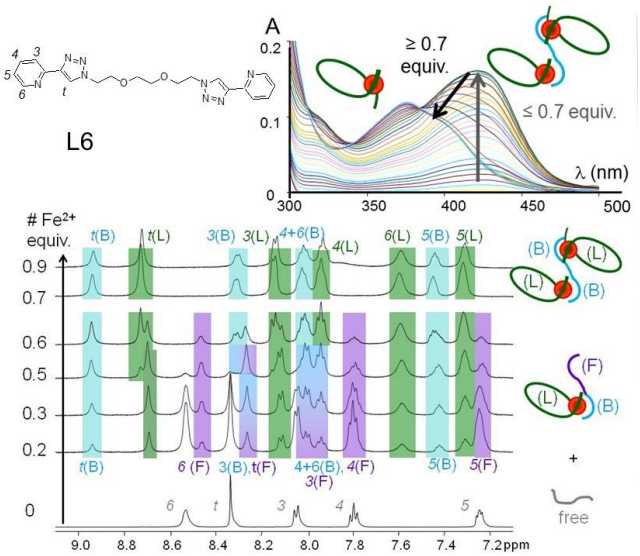

Fig. 6 Iron(II) titration to ligand **L6** monitored by UV-vis (top right, CH_3CN, 25 °C, [**L6**] 3.5×10^{-5} M) and by ^{1}H NMR spectroscopies (bottom, CD_3CN, 25 °C, [**L6**] 16 mM). (B) stands for 'bound', (L) for 'loop', (F) for 'free'.

Complexation of nickel(II) to **L6** leads to the sole formation of the 2:3 metal ion/ligand complex (Job plot with maximum at

x_{Ni2+}= 0.4, and sharp isosbestic points, ESI†). Zinc(II), on the other hand, leads to the very clean formation of a 1:1 complex which is likely an intramolecularly wrapped, tetrahedral-like complex, with strong binding (ESI†).

Self-assembly in the gas phase: influence of the spacer length analysed by mass spectrometry

Solution studies described above, in particular by ^{1}H NMR spectroscopy, give some insight into the structure of the self-assembled architectures, yet with limitations when mixtures are produced as in the case of **L2a** and **L4**, or when kinetic exchange takes place in an intermediate rate range where ^{1}H NMR signals are broad. In order to probe the nature of the self-assembled outputs, electrospray mass spectrometry was applied to the 3:2 ligand to iron(II) ion mixtures, at 10^{-4} M concentration (at lower concentrations, these architectures fall apart even under soft desolvation methods, as has been observed by others[6a]). Even at such significant concentration, extensive fragmentation is visible as mononuclear (in green) and double-stranded dinuclear (in pink) complexes are present with all ligands (Fig. 7). The ESI-MS analysis of these mixtures deserves several comments. First, the use of tetrafluoroborate counterions somewhat complicates the spectra because of its partial hydrolysis yielding fluoride anions. Because of the multiply charged nature of the iron(II) assemblies, various combinations of BF_4^- and F^- anions often produce several signals for the same cationic assembly. So although many peaks appear on the spectra, only a limited number of cationic assemblies are actually present. However, the presence of coordinating fluoride anions (compared to tetrafluoroborates) has the unintended benefit of providing some information about the coordination sphere of the ion in each assembly: assemblies whose m/z value point to complexes where the iron(II) centers are fully coordinated to pyridyl-triazole units display at least one peak corresponding to sole BF_4^- accompanying anions (as one would anticipate since no additional ligand would be required to complete the ion coordination sphere). However, when the m/z values correspond to complexes bearing only one or two pyridyl-triazole chelates, at least one fluoride accompanies the cationic assembly. This interesting piece of information correlates with the peak assignment determined based on m/z values and isotopic patterns.

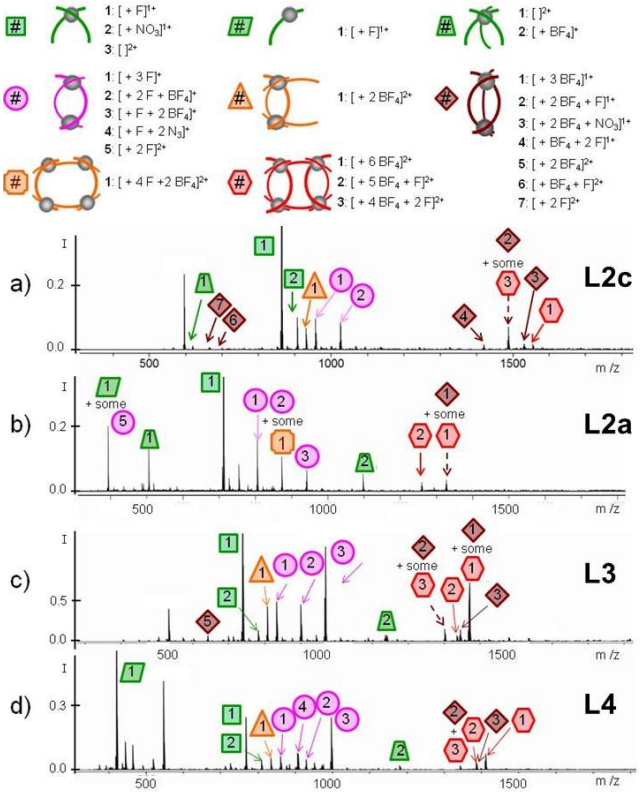

Fig. 7 ESI-MS analysis of 2:3 mixtures of $[Fe(H_2O)_6](BF_4)_2$ with ligands **L2c** (a), **L2a** (b), **L3** (c) and **L4** (d), in CH_3CN (25 °C). Peak assignment is shape and colour coded, as detailed on top. Each peak assignment was confirmed by its isotopic pattern.

When analysing the ESI-MS spectra in detail, the following families of assemblies are found: (i) triple-stranded dinuclear assemblies resembling the ones found in the solid state and characterized in solution by ^{1}H NMR, represented by brown diamonds in Fig. 7 are present in their 2+ state for **L2c** and **L3** and 1+ for all analysed ligands (**L2c**, **L2a**, **L3** and **L4**). However, the m/z section where 1+ signals of these triple-stranded assemblies appear contains significant amounts of the tetranuclear sextuple-stranded 2+ architecture (red hexagons in Fig. 7),[§] in particular for **L2a** and **L4** ligands. A zoom of this region is given in Fig. 8, together with a cartoon representations of the peak assignments. Considering that 2+ ions are intrinsically less represented in ESI-MS spectra than 1+ ion, their abundance in the gas phase analysis of **L2a** and **L4** complexes is striking, and correlates with their complex ^{1}H NMR behaviour compared to **L2c** and **L3** (Fig. 3).

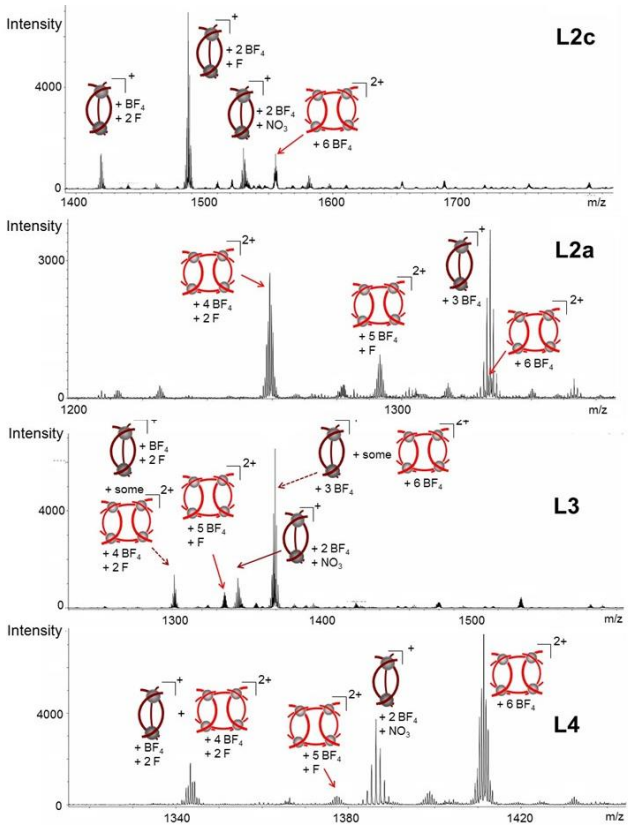

Fig. 8 ESI mass spectra between 1300-1600 g/mol for 2:3 mixtures of $[Fe(H_2O)_6](BF_4)_2$ with ligands **L2c**, **L2a**, **L3** and **L4**, in CH_3CN (25 °C). Each peak assignment was confirmed by its isotopic pattern.

Partially de-assembled hexamers are also observed in the ESI-MS spectra in the form of dinuclear quadruple-stranded complexes (orange triangles, Fig. 7), and tetranuclear quadruple-stranded architectures (orange distorted square, Fig. 7; note the association of four fluorides, as if one for each ion corner).

In summary, ESI-MS analysis complements and refines the ^{1}H NMR information above: ligands such as **L2c** and **L3** mostly select dinuclear triple-stranded architectures, while **L2a** and to a certain extent **L4** are prone to form larger architectures such as tetranuclear sextuple-stranded assemblies. As suggested by ^{1}H NMR, the **L2a** ligand seems more susceptible to poly-association, and this may be the result of a closer proximity of lone pairs of the 1,2,3-triazole 'middle' N2 nitrogen atoms, as discussed above. In the hexameric structure, this effect would be relieved in the ligand bridging the two dinuclear double-stranded portions, as illustrated by a model for one possible hexameric structure represented in ESI†.

Self-assembly in solution: influence of the spacer length analysed by vapour pressure osmometry

Although the ESI-MS analysis above provides precious, detailed information about the various architectures formed by these complexes by displaying the various m/z peaks corresponding to each individual assembly in the mixtures, the question of the desolvation effect remains. As shown by UV-vis analysis under dilute conditions (typically 10^{-5} M, see ESI† for details on each ligand), 2:3 iron(II)/ligand complexes with these ligands are very stable. Yet, it takes 10^{-4} M solutions to detect them after electrospray desolvation, and with significant fragmentation still. Therefore solution-phase mass assessment was explored using vapour pressure osmometry (VPO), looking for signs of larger assemblies in solution as well. Although a fairly old method which gives only average molecular weights and is complicated by the fact that these are charged, associative systems, VPO yields some additional qualitative information about the relative size of the assemblies (when comparing the various ligands together). The reader is invited to refer to reviews cited in reference 11 for details on VPO thermodynamics. For the purpose of this article, the most relevant expression relating the VPO response (electrical voltage imbalance) to the average molecular weight (M_{na}) and absolute charge ($|z|$) is given by equation Eq 1 below, for solutions where no supporting electrolyte was used.

$$\lim_{c \to 0} \left(\frac{E}{c}\right) = \frac{K_{vp}}{M_{app}} \qquad \text{where } M_{app} = \frac{M_{na}}{|z|+1}$$

Eq 1 VPO response as defined by E/c as a function of concentration. E is the electrical microvolt imbalance, which is proportional to the temperature difference between the two thermistors, c is the concentration in g of solute per kg of solvent, K_{vp} is a proportionality constant dependent on the apparatus, temperature and solvent, M_{na} is the average molecular weight of the solute, M_{app} is the apparent molecular weight of the solute, and $|z|$ its absolute charge.

The E/c ratio measured for iron(II) complexes with **L2a**, **L2c**, **L3** and **L4** is given in Fig. 9, and extrapolated to c = 0 g/kg by linear regression (dotted lines).

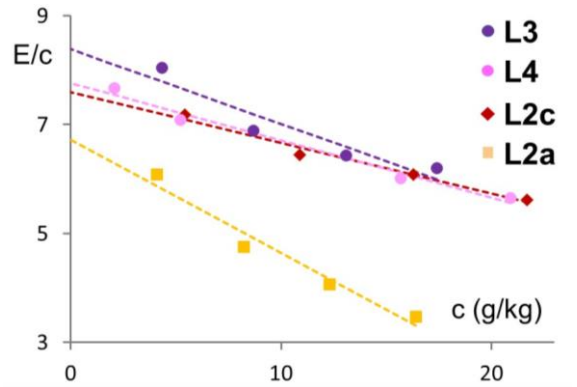

Fig. 9 VPO analysis of 2:3 mixtures of $[Fe(H_2O)_6](BF_4)_2$ with ligands **L2a**, **L2c**, **L3** and **L4** in CH_3CN (38 °C) at 10-40 mM ligand concentrations. E is the electrical microvolt imbalance,[11] c is the concentration in g/kg. Linear regression curves are indicated by dotted lines.

As indicated by Eq. 1, the y-intercept of the E/c *vs* c curves is inversely proportional to the apparent molecular weight M_{app}. Based on the y-intercepts of the E/c curves from Fig. 9, the M_{app} (*i.e.* $M_{na}/(|z|+1)$) ranking for the various complexes is therefore:

L2a > **L4** ~**L2c** > **L3** (VPO).

The expected molecular weights of the $[Fe_2(\mathbf{L})_3]^{4+}$cations follow the following trend:

L2c > **L4** > **L3** > **L2a** (M_w).

The VPO measurements therefore highlight two features:

(i) **L2a** ligand yields architectures with the largest M_{app} as measured, when it would be expected to generate the lightest dinuclear triple-stranded architectures based on calculated molecular weights. A larger M_{app} results either from a larger M_{na}

or from a smaller charge |z|. However, UV-vis titrations indicate that 2:3 iron(II)/ligand complexes are formed with all ligands, so the charge of all these assemblies is at least 4+. A larger charge would artificially reduce M_{app}. However, in **L2a**'s case, the M_{app} is surprisingly larger than anticipated (not smaller). This means that **L2a** forms heavier assemblies, a result that correlates with species observed by ESI-MS: the tetranuclear quadruple-stranded species (orange distorted square, Fig. 7), and the tetranuclear sextuple-stranded complex (red hexagons, Fig. 7, and red cartoons, Fig. 8). These two larger species increase M_{app} through their significantly larger molecular weight, while decreasing M_{app} through their higher charge (8+). The overall effect is still a larger M_{app} reflected by a smaller y-intercept for **L2a**.

(ii) Some similarity is observed with **L4**-derived complexes, although at a much smaller scale. Indeed, a dinuclear triple-stranded $[Fe_2(\mathbf{L4})_3]^{4+}$ complex would have a smaller calculated molecular weight than its **L2c** counterpart. However their respective VPO signals are nearly superimposable, meaning that M_{app} for **L4** is larger than expected for $[Fe_2(\mathbf{L4})_3]^{4+}$cations. Once again, this correlates with a larger proportion of higher-degree assemblies for **L4** than for **L2c** as observed by ESI-MS (sextuple-stranded assemblies, Fig. 7,8) and by ^{1}H NMR (small side-product peaks). However, as anticipated from the ^{1}H NMR signals, the proportion of these higher oligomers in the case of **L4** is minimal, which correlates with the small effect on its VPO response compared to **L2a**.

All in all, VPO measurements confirm that the higher assemblies observed in the gas phase by ESI-MS impact the species distribution in solution as well. Both aliphatic ligands with an even number of carbon atoms in their spacer are affected, with the effect on the shorter ethylene spacer being more substantial than that of the butylene spacer, as also observed by ^{1}H NMR. This 'even number' effect does not seem to be restricted to the ethylene and butylene spacers, and the hexylene spacer was also reported to form higher aggregates as observed by ^{1}H NMR.[6a]

Self-assembly in solution: influence of the terminal pyridine

Beyond the effect of the spacer on the stability of dinuclear triple-stranded architectures, another element which may impact the self-assembly process is the substitution pattern of the most robust binding site within the chelate, which is, in the present case, the terminal pyridine. Generally speaking, the triazole unit is a much weaker ligand than pyridine, affinity-wise,[3e] as we have comparatively studied for Cu(I) complexes.[4b] By introducing a substituent in the 6-position of the pyridyl, we could investigate the extent of destabilization of the derived dinuclear species, and the role that the spacer plays in accommodating the steric hindrance to coordination that is enforced by the methyl group. A new chelating unit was therefore synthesized through the cycloaddition of 2-ethynyl-6-methylpyridine[12] with diazides prepared *in-situ* by the S_N2 reaction of sodium azide onto dibromides (ESI†). The dibromides, which dictate the properties of the spacer in the final ligands, were restricted to the *p*-xylyl, propylene and butylene fragments for which the analogues without methyl groups form the best defined and most stable Ni(II) and Fe(II) complexes, as reported above. The discussion below will therefore be limited to methyl-bearing **L3M**, **L4M** and **L2cM** ligands which are methylated analogues of the propylene-derived (**L3**), butylene-derived (**L4**) and *p*-xylyl-derived (**L2c**) ligands, respectively (Scheme 1). The methylated monofunctional ligand **L1M** was also prepared as a reference.

In the family of methylated ligands, **L3M** with the shortest tested spacer suffers the most destabilization in both iron(II) and nickel(II) binding, with a much more significant impact on iron(II) coordination (Fig. 10). Job plots with maxima between 0.4 and 0.5 confirm the coexistence of 2:3 and 2:2 complexes (ESI†).¶ Elongating the alkyl spacer by one more methylene group (as in **L4M**), however, restores very good to excellent affinity to iron(II) and nickel(II) respectively, and a 2:3 metal/ligand stoichiometry (Fig. 10 and Job plot in ESI†). It therefore appears that a four methylene unit brings sufficient flexibility from the spacer for the dinuclear complex to better accommodate the end-group strain imposed by the methyl group. Moving away from a purely aliphatic spacer, ligand **L2cM** with a *p*-xylyl spacer is more conformationally restricted because of just two methylene groups. However, it offers more stabilizing effects with possible edge-to-face π-π interactions between spacers, as suggested by the CPK representation of the $[Fe_2(\mathbf{L2c})_3](BF_4)_4$ and $[Ni_2(\mathbf{L2c})_3](BF_4)_4$ crystal data, and by the more sigmoidal UV-vis titration curves of **L2cM** with Ni(II) and Fe(II) compared to the aliphatic-based spacers (the comparison of UV-vis data between **L2cM** and **L4M**/**L3M** is presented in ESI† for the sake of clarity). This may explain why **L2cM**'s binding is stronger than **L3M**'s, but weaker than **L4M**'s. Unfortunately, in our hands all attempts to prepare single crystal suitable for X-ray crystallography to probe the coordination sphere and spacer involvement with methylated ligand-based complexes failed. Overall, the end-strain induced by a methyl group in the 6-position of a pyridine is easily accommodated by a flexible spacer composed of at least four methylene groups. A more rigid propylene spacer still forms the 2:3 metal/ligand complex yet with a weaker affinity. However, rigidity can be compensated for by additional interaction between spacer groups, as in **L2cM**. Not surprisingly, end-group strain affects iron(II) complexes more than their nickel(II) counterparts because of iron(II)'s intrinsic weaker affinity to pyridyl-type ligands.

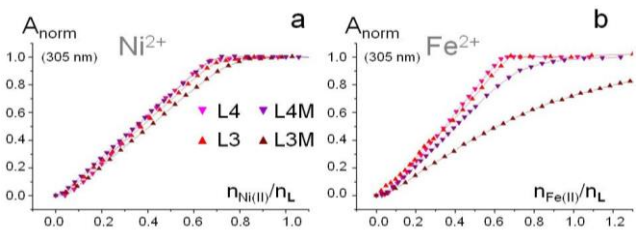

Fig. 10 Comparative UV-vis titration profiles of (a) nickel(II) and (b) iron(II) to methylated (**L3M**, **L4M**) and non-methylated (**L3**, **L4**) bifunctional ligands (CH_3CN, 25 °C).

ESI-MS analysis was also conducted on iron(II) complexes of **L2cM**, **L3M** and **L4M** ligands at 10^{-4} M, but not surprisingly the observed signals mostly correspond to dissociated assemblies (ESI†, Fig. S64). VPO also reflects complex dissociation, with a smaller M_{app} for both the **L3M** and **L4M** complexes (**L2cM** did not give complexes that were soluble enough in CH_3CN for VPO analysis; see Fig. S65 in ESI†).

Magnetic properties

Iron(II) complexes are of particular interest due to the richness of their magnetic properties. Indeed, depending on the balance between the field strength and electron pairing energy, these d^6 transition metal ions may occupy high-spin (paramagnetic, S = 2) and low-spin (diamagnetic, S = 0) states. More interestingly, complexes involving ligands of intermediate field strength may switch between these two states under the influence of external stimuli, a category known as 'spin cross-over' (SCO) complexes.[6a] In this context, the 1,2,3-triazole-pyridine diad is of particular interest since it combines the strong-field pyridine ligand with the weak-field 1,2,3-triazole unit. Additionally, the ligand field of a pyridine is decreased upon introduction of a methyl group in its 6-position, allowing to favour a transition to a higher spin in species prone to forming low spin complexes with ligands such as phenanthrolines and 2,2'-bipyridine.[14a]

Hence, the spin state of 1,2,3-triazole-pyridine-based iron(II) complexes was explored theoretically and experimentally in mononuclear compounds derived from ligands **L1** and **L1M**. Furthermore, the experimental study of the dinuclear systems allows assessing the impact of the spacer, its rigidity or induced relative chirality at the metal ion centers on potential spin cross-over to be investigated.

Electronic effects studied by UV-vis spectroscopy and DFT in mononuclear complexes

As in iron(II) tris(2,2'-bipyridine) complexes, the tris(1,2,3-triazolylpyridine) iron(II) complexes are intensely coloured (dark orange to red) as quantified by a relatively strong absorption in the visible region (λ_{max} at 425 nm, Fig. 11a for $[Fe(\mathbf{L1})_3]^{2+}$). DFT calculations confirm the metal-to-ligand charge transfer nature of the bands in the visible region for a low-spin species (Fig. 11b). In the DFT-calculated spectrum of the low spin complex (Fig. 11b), absorption at the highest wavelength (around 450 nm) involves a metal-to-pyridine charge transfer, whereas a separate metal-to-triazole charge transfer is calculated to occur at higher energy (corresponding to a λ_{max} around 310 nm). In the experimental spectrum of $[Fe(\mathbf{L1})_3](BF_4)_2$ (Fig. 11a), these transitions are merged into a broad series of absorptions over about 100 nm. Together with the well-defined ^{1}H NMR spectrum and X-ray structure at 180 K, the UV-vis data confirm the formation of a low-spin mononuclear complex in $[Fe(\mathbf{L1})_3](BF_4)_2$. This is consistent with a DFT-derived 28.9 kcal/mol stabilization of the low-spin complex *vs* its high-spin counterpart with 1,2,3-triazolylpyridine chelates where the pyridine position 6 is occupied by a hydrogen. However, the introduction of a methyl group *ortho* to the nitrogen of the pyridine is known to weaken the ligand field. Experimentally, the $[Fe(\mathbf{L1M})_3](BF_4)_2$ complex was indeed shown to be high-spin at room temperature, as indicated by its very broad ^{1}H NMR spectrum over an extended chemical shift range (ESI†) and by SQUID measurements (see below Fig. 13a). The absorption of the yellow complex $[Fe(\mathbf{L1M})_3](BF_4)_2$ also displays a shoulder between 300 and 320 nm consistent with the DFT calculations of an iron(II) tris(pyridyl-1,2,3-triazol) complex in the high-spin state (Fig. 11b).

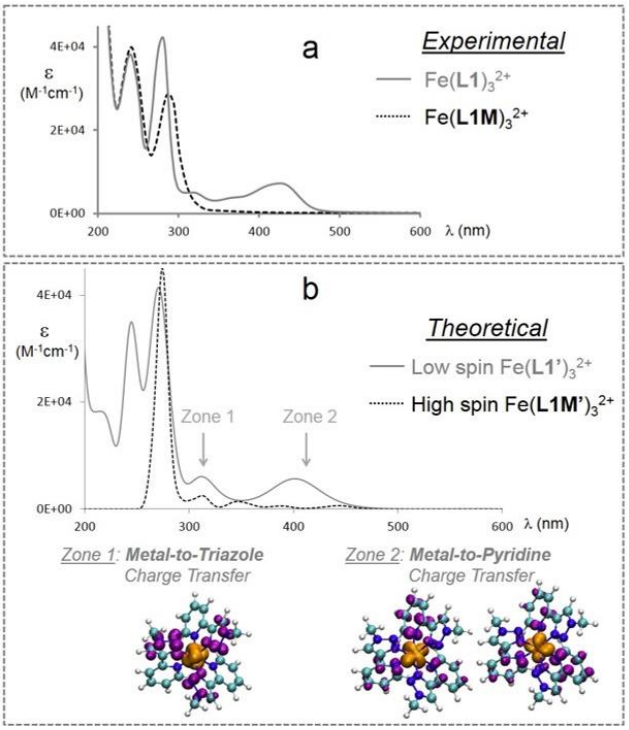

Fig. 11 a) Measured experimental and b) TD-DFT-derived theoretical UV-vis spectra of high-spin and low-spin iron(II) mononuclear complexes. The experimental spectra in a) were collected for the synthesized $[Fe(\mathbf{L1})_3](BF_4)_2$ and $[Fe(\mathbf{L1M})_3](BF_4)_2$ complexes in acetonitrile (4×10^{-5} M, 25 °C). DFT calculations for high-spin and low-spin complexes were performed based on a monofunctional ligand similar to **L1** except for the benzyl group which was replaced by a methyl group to save calculation time. Under the spectra are represented the charge density differences between the excited and the ground states (increase in purple, decrease in orange; details in ESI†).

Although efforts to crystallize $[Fe(\mathbf{L1M})_3](BF_4)_2$ have been unsuccessful, geometry optimization of $[Fe(\mathbf{L1M'})_3]^{2+}$ by DFT offers some insight into its structure (in **L1M'**, a methyl group replaces the benzyl unit). Among the four forms of high-spin, low-spin, *fac* and *mer* $[Fe(\mathbf{L1M'})_3]^{2+}$ isomer, the *mer* complex is significantly more stable (the calculated relative energy levels are given in ESI†), with the high-spin complex favoured by more than 1.8 kcal/mol (ESI†). In the *fac* complexes, the substituent in position 6 of one pyridine points towards the center of another pyridine ring. This is easily accommodated in an unsubstituted pyridine, such as in $[Fe(\mathbf{L1})_3]^{2+}$ (H on pyridine position 6) which displays a *fac* arrangement in the crystal state (Fig. 12c).[3g] However, 6-methyl-substituted pyridines suffer from significant steric congestion when all three methyl groups are stacked against adjacent pyridines in the *fac* trimethylated complex (*mer* $[Fe(\mathbf{L1M'})_3]^{2+}$ is represented in Fig. 12a, and its *fac* isomer appears in Fig. 12b). Similar *mer* selection has been observed in the crystal state of iron(II) tris(6-methyl-2,2'-bipyridine) which also displays high-spin properties.[13b]

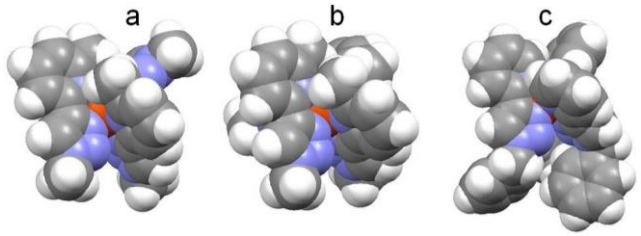

Fig. 12 Comparative CPK representation of a) DFT-optimized high-spin *mer* $[Fe(\mathbf{L1M'})_3]^{2+}$, b) DFT-optimized high-spin *fac* $[Fe(\mathbf{L1M'})_3]^{2+}$ and c) crystallographic low-spin *fac* $[Fe(\mathbf{L1})_3]^{2+}$.[3g]

Low-spin and high-spin states in iron(II) dinuclear complexes

With the characteristics of the low and high-spin iron(II) complexes in hand, it is interesting to explore the behaviour of the dinuclear species and the role of the spacer on the magnetic properties. Dinuclear iron(II) complexes have attracted significant attention due to possible cooperativity/anti-cooperativity in spin cross-over around each metal center,[13c-h] and the potential effect of guest binding on spin cross-over in these architectures.[13i-k] Many of these dinuclear systems involve the spin cross-over prone imidazole-imine chelate, and the magnetic behaviour of triazolyl-pyridine iron(II) complexes has not been reported to our knowledge.

Like their mononuclear analogue, the dinuclear iron(II) complexes derived from the methyl bearing ligands only show high-spin properties in the solid state, irrespective of temperature (Fig. 13a). The presence of the methyl group on the tightest binding element of the chelating unit dramatically weakens the ligand field to the point where the low-spin species is no longer accessible. This is reminiscent of the transition to an exclusive iron(II) high-spin state when one methyl group is introduced in 2,2'-bipyridine ligands (leading to 6-methyl-2,2'-bipyridine),[13b] as well as in mono- and di-nuclear benzimidazolylpyridines.[13c]

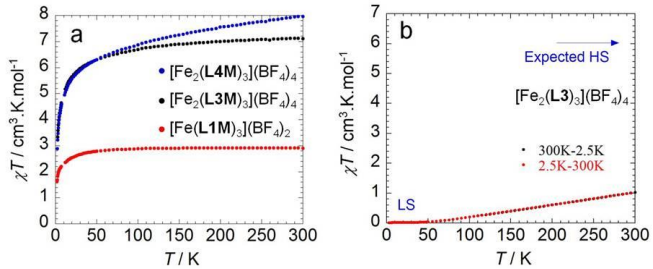

Fig. 13 SQUID measurements for iron(II) complexes of a) methyl- (**L1M**, **L3M**, **L4M**) and b) non-methyl-bearing (**L3**) ligands. $[Fe_2(\mathbf{L3})_3](BF_4)_4$ was measured in the crystalline state, while $[Fe(\mathbf{L1M})_3](BF_4)_2$, $[Fe_2(\mathbf{L3M})_3](BF_4)_4$ and $[Fe_2(\mathbf{L4M})_3](BF_4)_4$ were studied as powders.

Most of the non-methylated ligands induce low-spin iron(II) complexes as evidenced by their MLCT in UV-vis spectra, well-resolved ^{1}H NMR signature and SQUID measurement (**L2c**), similarly to their mononuclear analogue $[Fe(\mathbf{L1})_3](BF_4)_2$. However, the propylene bridged $[Fe_2(\mathbf{L3})_3](BF_4)_4$ complex displays a unique behaviour with possible spin cross-over properties. Polycrystalline $[Fe_2(\mathbf{L3})_3](BF_4)_4$ samples were studied by SQUID between 1.8 and 375 K (Fig. 13b illustrates the 2.5-300 K range). At 2.5 K, the χT product is 0.01 cm^3 K mol^{-1} which corresponds to a low-spin Fe^{II} ($S = 0$). As the temperature increases above 50 K, the χT product increases gradually to 1.03 cm^3Kmol^{-1} at 300 K which would be consistent with gradual spin crossover from a diamagnetic low-spin to a high-spin $S = 2$ Fe^{II} ion. It is noteworthy that the magnetic susceptibility data from 2.5-300 K is identical to that measured from 300-2.5 K with no thermal hysteresis. However, the full transition cannot be observed in the temperature range investigated, and no clear sigmoidal signature is observed. As a result, SCO may be occurring at higher temperatures; yet, access to higher temperatures would be necessary to unambiguously confirm SCO. In the literature, gradual and only partial spin cross-over with full conversion above 300 K has also been observed with mono-nuclear triazole-based iron(II) complexes bearing two terdentate triazole-pyridine-pyrazole ligands and tetrafluoroborate counterions.[13l,m]

The unique magnetic behaviour shown by $[Fe_2(\mathbf{L3})_3](BF_4)_4$ by SQUID correlates with a particular ageing effect of solutions of this sample, as observed by both UV-vis and ^{1}H NMR spectroscopies. Freshly preparing the triple-stranded complex by mixing **L3** (3 equiv.) with $[Fe(H_2O)_6](BF_4)_2$ (2 equiv.) in acetonitrile gives well-resolved ^{1}H NMR signals (Fig. 3) as well as a UV-vis signature typical of a low spin complex with MLCT character (ESI†). However, letting the solution age over 3 days induces a change to very broad ^{1}H NMR signals and loss of the MLCT band at 425 nm in favour of a broad band around 350 nm, consistent with a dominant high-spin species (the comparative data is represented in ESI†, Fig. S36, and DFT calculated high-spin spectrum for a mononuclear complex model is displayed in Fig. 11b). The single crystals grown over a week under argon for X-ray crystallography and used for SQUID experiments also show the signature of the aged complex when analysed in solution by ^{1}H NMR and UV-vis spectroscopies. The exact reasons why a transition to high-spin in aged solutions and crystalline samples is observed are still under investigation. None of the other bifunctional ligands bridged by aliphatic spacers (**L2a**, **L4**, **L5**) showed the same behaviour (no ageing effect as studied by ^{1}H NMR and UV-vis spectroscopies, ESI†).

Because spin cross-over relates to the strength of the ligand field, the UV-vis analysis of the nickel(II) complexes, which gives access to the 10Dq parameter in pseudo-octahedral complexes, provides some insight into the possibility of SCO and relative ligand field strengths. As apparent from Fig 14a and Table 1, all non-methyl-bearing ligands give nickel(II) complexes with maximum absorption around 870 nm and 10Dq(Ni^{2+}) well within the range of 11,200-12,400 cm^{-1} where SCO for Fe^{2+} species is considered accessible.[13a] The introduction of a methyl group induces a significantly weaker field (10Dq(Ni^{2+})~10.3 × 10^3 cm^{-1} for a 970 nm absorption, Fig. 14b, Table 1) consistent with lack of spin cross-over.

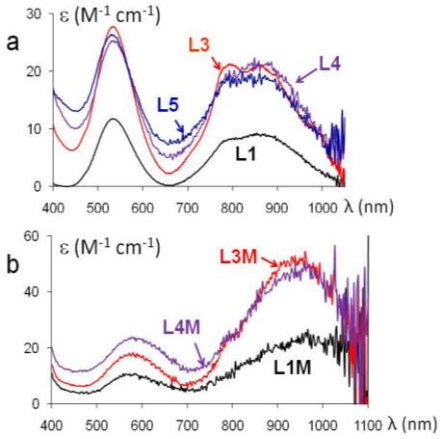

Fig. 14 NIR absorption of nickel(II) complexes of a) **L1**, **L3**, **L4** and **L5** (2-5 mM), and b) **L1M**, **L3M**, **L4M** (0.8 mM) in acetonitrile, 25 °C.

Table 1 NIR absorption data for $[Ni(\mathbf{L})_3](BF_4)_2$ (**L**= **L1**, **L1M**) and $[Ni_2(\mathbf{L})_3](BF_4)_4$ (**L**= **L3**, **L4**, **L5**, **L3M**, **L4M**) in acetonitrile (25 °C).

X	**L1**	**L3**	**L4**	**L5**	**L1M**	**L3M**	**L4M**
λ_{max} (nm)	875[a]	865[b]	870[a]	870[a]	970[a]	960[a]	970[a]
$10Dq_{Ni}$ (cm^{-1})	11,430[c]	11,560[d]	11,495[c]	11,495[c]	10,310[e]	10,420[e]	10,310[e]

[a] ± 10 nm; [b] ± 5 nm; [c] ± 130 cm^{-1}; [d] ± 65 cm^{-1};[e] ± 110 cm^{-1}.

As seen from the very similar values of NIR absorption in nickel(II) complexes with hydrogen-bearing pyridines, the unique possible SCO behaviour of $[Fe_2(\mathbf{L3})_3](BF_4)_4$ may not be simply explained by the sole effect of the ligand field. In the solid state, weak interactions responsible for crystal packing of $[Fe_2(\mathbf{L3})_3](BF_4)_4$ fully described in reference 4g induce the closest lateral packing of all the crystallized dinuclear complexes (and shortest ion-ion distance) in all the resolved crystal structures (9.9 Å in $[Fe_2(\mathbf{L3})_3](BF_4)_4$ *vs* 11.4 Å in $[Fe_2(\mathbf{L2c})_3](BF_4)_4$ and 13.4 Å in $[Fe_2(\mathbf{L2d})_3](BF_4)_4$),[4g] and may provide a pathway for the effective ligand field to be further tuned.

Selection of self-assembled architectures

Double-stranded *vs* triple-stranded systems

Self-sorting of self-assembled architectures from a mixture of components has been a subject of intense studies,[7] probably driven by the awe-inspiring self-assembly of countless materials into cells.[14a-c] In this context, the pyridyl-triazole chelate, although a weaker ligand than 2,2'-bipyridine, also is a candidate for specific selection of double-stranded *vs* triple-stranded architectures. The selection process may be dictated by:

- the metal ion's geometrical preference,
- the ligand's features including (i) the steric hindrance displayed at its end where coordination takes place (methylated *vs* non-methylated pyridine) and (ii) the particular properties of the spacer (short spacer as in **L2a** *vs* longer spacer as in **L2c**). Both of these aspects are explored below.

End-strain effect: methylated vs non-methylated pyridine.

As discussed above, the presence of a methyl group on position 6 of the terminal pyridine limits the ability of the pyridyl-triazole unit to form very stable octahedral complexes within dinuclear structures. On the one hand, the presence of the methyl group in **L2cM** for instance is not easily accommodated in a rigid octahedral environment (octahedral iron(II)), but would provide limited steric hindrance in the tetrahedral context of a double-stranded species. On the other hand, non-methylated ligand **L2c** which does not display steric hindrance gives a very stable triple-stranded species in the presence of Fe^{2+}. As a result, self-selection would be expected in a mixture of **L2c**, **L2cM**, Fe^{2+} and Cu^{+}, giving exclusively the triple-stranded $[Fe_2(\mathbf{L2c})_3]^{4+}$ and double-stranded $[Cu_2(\mathbf{L2cM})_2]^{2+}$ outcome. ^{1}H NMR confirms this hypothesis, as evidenced in Fig. 15. Fig. 15a gives the ^{1}H NMR signature of a 2:2 **L2cM**/Cu^{+} mixture, corresponding to the $[Cu_2(\mathbf{L2cM})_2](BF_4)_2$ chemical formula determined by elemental analysis (ESI†). The signature of $[Fe_2(\mathbf{L2c})_3]^{4+}$ is repeated in Fig. 15b. The 3:2:2:2 mixture of **L2c**, **L2cM**, Fe^{2+} and Cu^{+} analysed in Fig. 15c confirms the sole formation of the self-selected $[Fe_2(\mathbf{L2c})_3]^{4+}$ and $[Cu_2(\mathbf{L2cM})_2]^{2+}$ complexes, as the spectrum of the mixture is exactly the superimposition of that of the two individual architectures. Such discrimination provided by a methyl group in the 6-position of a pyridine, which destabilizes the formation of octahedral complexes while leaving the stability of tetrahedral geometries where the two chelate ligands are orthogonal to each other unaffected, has precedents in the 2,2'-bipyridine helicate literature.[14d]

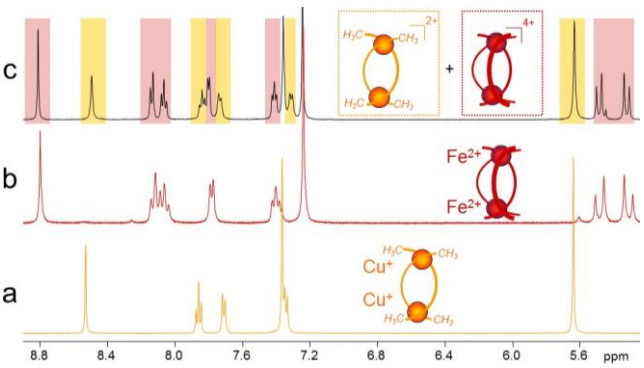

Fig. 15 Self-selection of double-stranded copper(I) *vs* triple-stranded iron(II) architectures evidenced by ^{1}H NMR of a 3:2:2:2 mixture of **L2c**, **L2cM**, $[Cu(CH_3CN)_4]BF_4$ and $[Fe(H_2O)_6](BF_4)_2$ (CD_3CN, 25 °C, 500 MHz for a**)** and c), 400 MHz for b)).

Spacer-strain effect: short vs long spacer.

In the example above, the central spacer is identical in both **L2c** and **L2cM**, ligands, and the end-strain was used to screen octahedral *vs* tetrahedral environments, as in the 2,2'-bipyridine family. However, the pyridyl-triazole unit offers an alternative handle to screen triple-stranded architectures: as discussed in the above sections in gas and solution phases, the very short ethylene spacer in **L2a** is characterized by destabilized triple-stranded dinuclear iron(II) assemblies, likely resulting from the proximity of the triazole 'middle' nitrogen of each metal ion center. This would be expected to be particularly sensitive with metal ions with strictly octahedral geometry such as iron(II). However, ions with more flexible geometry, or even more variety in their coordination numbers, would likely well tolerate the **L2a** ligand. Therefore we explored the possible self-selection of triple-stranded dinuclear helicates with well-spaced pyridyl-triazole chelates (such as in the *p*-xylyl based **L2c** ligand) away from dinuclear architectures based on the more compact **L2a** ligand, using iron(II) as a source of a strict octahedral environment, and

zinc(II) as a more flexible metal ion. ^{1}H NMR analysis of the 3:2:2:2 mixture of **L2c**/**L2a**/Zn^{II}/Fe^{II} is represented in Fig. 16.

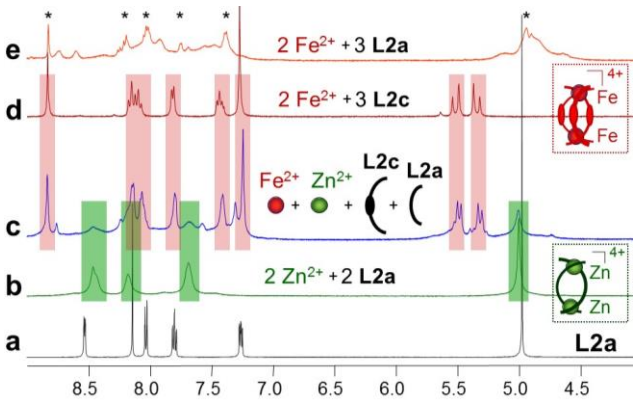

Fig. 16 Self-selection of zinc(II) *vs* iron(II) architectures based on spacer length explored by ^{1}H NMR of a 3:2:2:2 mixture of **L2c**, **L2a**, $Zn(OTf)_2$and $[Fe(H_2O)_6](BF_4)_2$ (CD_3CN, 25 °C, 500 MHz, [**L**] ~ 20-30 mM): a) **L2a** alone; b) **L2a** signals after addition of one equivalent of $Zn(OTf)_2$ (with respect to **L2a**); c) after further addition of **L2c** (1.5 equiv.) and $[Fe(H_2O)_6](BF_4)_2$ (1 equiv.). For comparison, ^{1}H NMR of $[Fe_2(\mathbf{L2c})_3]^{4+}$ (400 MHz, d), and 3:2 mixtures of **L2a** and $[Fe(H_2O)_6](BF_4)_2$ (300 MHz, e) are given in CD_3CN (in e, asterisks signal what was identified as the triple-stranded $[Fe_2(\mathbf{L2a})_3]^{4+}$ complexes; see Fig. 3).

Although the selection is not as dramatic as in the previous section due to the slow precipitation of the self-assemble zinc(II) complex leading to loss and broadening of signals, a few features are worth highlighting. First, in the four component mixture (Fig. 16c), a major component appears to be the triple-stranded *p*-xylyl-based $[Fe_2(\mathbf{L2c})_3]^{4+}$ complex, as evidenced by the aromatic and benzylic protons at chemical shifts identical to those of pure $[Fe_2(\mathbf{L2c})_3]^{4+}$ (Fig. 16d; red bands). In the four component mixture (Fig. 16c), ligand **L2a** seems to be very much involved in the same zinc complex as in a simple 2:2 mixture with Zn(II) (Fig. 16b, green bands), although partial precipitation of this complex reduces its signals' intensity. Interestingly, the very complex and broad signature of a 2:2 mixture between Fe^{2+} and **L2a** alone (Fig. 16e, particularly visible in the α CH_2 and H5 regions; see Fig. 3 for labelling) does not seem to be present, suggesting that there is indeed segregation of Fe^{2+} with **L2c**. This self-selection process does not lead to totally orthogonal binding of Fe^{2+} with **L2c**, and Zn^{2+} with **L2a**, however, as a well-defined minor component appears to be present, with small signals of what seems to involve the **L2c** ligand (*e.g.* minor triazole proton at 8.76 ppm, and minor diastereotopic protons in the 5.2−5.6 ppm region, Fig. 16c). These may be related to a mixed hexameric assembly with **L2a** bridging ligands, as observed by ESI-MS with **L2a** alone (Fig. 7 and 8), although more work would need to be done to explore such hybrid structure. In summary, although discrimination is not perfect under the explored conditions, this example shows that pyridyl-triazole ligands with spacers of various lengths can be used to direct preferential self-assembly and self-selection.

Double-stranded *vs* loop architectures

The above example uses the spacer length as the guiding information for selection, with **L2a** and **L2c** which are both semi-rigid strands. In another approach, we explored the effect of the flexibility of the spacer in directing the selection of 'loop' *vs* helicate architectures, in the presence of ions of flexible or stricter geometrical preferences (*e.g.* Zn^{2+} *vs* Cu^+). Using **L2c** as semi-rigid and **L6** as semi-flexible ligands respectively, we wanted to see if any binding selectivity would be shown towards Cu^+ and Zn^{2+}, knowing that the semi-rigid **L6** ligand accommodates the flexible zinc ion into a loop structure very well (see above), and that copper(I)'s fairly strict tetrahedral geometry is well tolerated by **L2c** into a 2:2 complex. This is an intrinsically difficult challenge, as a mono-nuclear looped structure comes from a simple bimolecular event, whereas the formation of a dinuclear double-stranded structure involves bringing four independent components together, and therefore is entropically much more costly. So not surprisingly the selection process is not as clear cut as above, it still brings some valuable information highlighted below.

When a 1:1:1:1 solution of **L6**/**L2c**/$Zn(OTf)_2$/$Cu(CH_3CN)_4BF_4$ in acetonitrile was analysed by ESI-mass spectrometry (Fig. 17),[#] the most intense peaks indicate the selection of zinc complexes with the loop ligand **L6** only ($[Zn\mathbf{L6}]^{2+}$ ion at m/z 235.06 and the 1+ triflate species at 619.07, Fig. 17, confirmed by the isotopic pattern[‡]). This is consistent with the very stable 1:1 Zn/**L6** complex observed by UV-vis titrations with **L6** alone (see above and ESI†). Maybe not surprisingly, the loop complex with Cu^+ is also present in the mixture as indicated by the peak at 469.11 corresponding to $[Cu\mathbf{L6}]^+$. Indeed, the low entropic cost for the formation of a 1+1 complex *vs* a 2+2 dinuclear assembly combined likely over-rides the enthalpic cost associated with the steric strain that the semi-flexible loop **L6** provides to the strictly tetrahedral Cu^+ ions. So overall it is not surprising to detect the $[Cu\mathbf{L6}]^+$ ion in the gas phase. Interestingly, only the copper(I) xylyl-based complexes appear at significant levels, with signals at 457.09 (2+), 1001.20 and 1065.14 (1+ with BF_4 and OTf counterions, respectively). A Cu^+ 'corner' involving two xylyl-based ligands **L2c** is also present with a signal at 851.26 (Fig. 17a). One could argue that the zinc complexes with **L2c** may just not be observed by mass spectrometry due lower stability. However, a close inspection of the area where the 2:2 and 2:3 zinc(II)/**L2c** species would appear leads to the detection of several of the expected zinc complexes, although at very low abundance, showing that they do withstand ESI-MS analysis, but are very minor species. All the peaks of very low abundance in the dinuclear zinc complex region could be assigned on the basis of the m/z values and isotopic patterns. A zoomed spectrum on the relevant area with 100 times magnification compared to Fig. 17a is represented in Fig. 17b, and shows some interesting features. First, very minute amounts of triple-stranded zinc complexes are present, in an all-**L2c** homoleptic $[Zn_2(\mathbf{L2c})_3]^{4+}$or heterolepic $[Zn_2(\mathbf{L2c})_2(\mathbf{L6})]^{4+}$ format. At least two semi-rigid **L2c** are required to form this type of triple-stranded dinuclear complex. Among these very minor products, double-stranded mixed complexes (one Cu^+ and one Zn^{2+}) including at least one semi-rigid **L2c** ligand are more abundant. Finally, what was assigned as a loop dimer bridged by triflates is also detected (this interpretation is inspired by zinc's intrinsic oxophilicity as well as by the coordination properties of **L6** with Fe^{2+}, as seen above, Fig. 6).

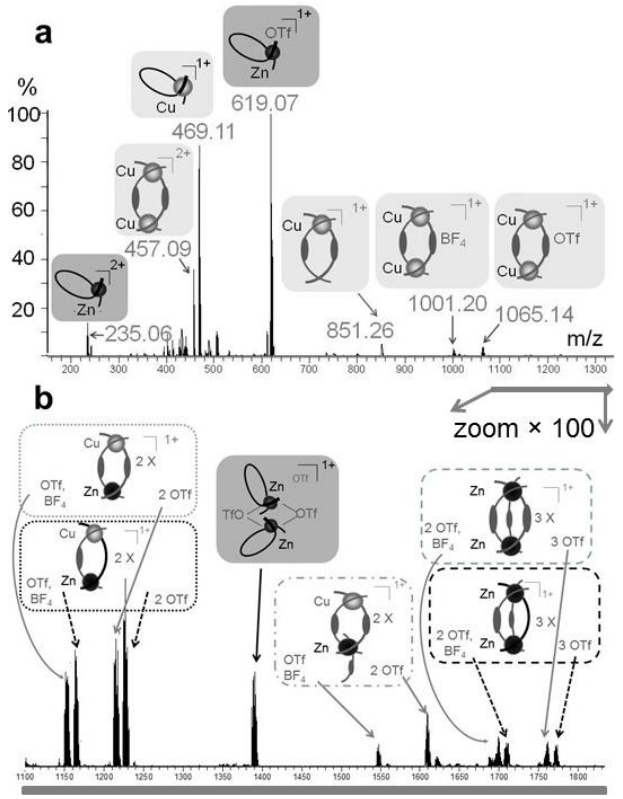

Fig. 17 Selection of double-stranded Cu^{+} dinuclear complexes *vs* Zn^{2+} and Cu^{+} metallo-loops observed by ESI mass spectrometry. Black lines represent oligoether ligand **L6**. Grey lines with a bulge represent the *p*-xylyl spacer in **L2c** ligands. a) Full spectrum, b) zoom on region where 2:2 and 2:3 zinc(II)/**L2c** species would appear. In the boxes, 'X' stands for 'counteranion' which is then specified at the bottom left and right of each box.

Conclusions

Although the pyridyl-triazole diad may in first approximation be seen as a synthetically convenient alternative to the classical 2,2'-bipyridine coordination chelate, the systematic study described in this manuscript highlights its original own features. More specifically:

1 The particular orientation of the nitrogen N2 lone-pairs of the 1,2,3-triazole unit, pointing towards the cavity of triple-stranded dinuclear complexes, seems to destabilize these particular architectures when small ethylene spacers are involved, and populate larger architectures. Such spacer sensitivity distinguishes the pyridyl-triazole diad from the 2,2'-bipyridine chelate. In this context, the intriguing cyclic hexamers detected by mass spectrometry are certainly worthy of further exploration, as they may allow access to increased complexity in the self-assembly process (*e.g.* selection of architectures with mixed ligand and mixed metal ions). Preliminary examples of self-selection are already emerging.

2 Structurally speaking, semi-rigid bifunctional ligands yield triple-stranded dinuclear structures with iron(II) and nickel(II) under non-competitive conditions (non-coordinating anions), and follow the 'even/odd' helicate/mesocate rule observed with bipyridine and catechol chelates. However, the flexibility of the triazole-spacer hinge is such that both helicate and mesocate structures start to be nearly equally populated as early as in the pentylene spacer.

3 Due to its weaker ligand field, the pyridyl-triazole diad may open the door to spin-cross over properties, controlled by the chemical nature and length of the spacer. The propylene spacer is of particular interest, and further studies need to be conducted to fully understand the details of its magnetic behaviour, for instance its ageing effect and slow magnetic conversion. With regards to the latter point, changing the tetrafluoroborate with a perchlorate was shown in the literature to transform a gradual, high-temperature spin cross-over into a complete, lower temperature conversion of iron(II) complexes bound to triazole-involving terdentate ligands,[13l] so exploring counterion effects on iron(II) complexes of all the non-methylated ligand family would be the first measure to take.

Overall, with such a convenient synthetic access and rich physical and chemical properties, the pyridyl-triazole diad embedded in polyfunctional ligands is certainly only starting to reveal its potential.

Acknowledgments

The authors thank Prof. Louis Cuccia for his precious help with and access to the VPO equipment, and the reviewers for their time and attention provided to this long manuscript, as well as their suggestions. The authors are also indebted to Dr Gabriele Schatte for her assistance in the analysis of X-ray diffraction data. Funding from the Natural Sciences and Engineering Research Council of Canada (USRA for N.W and D.G. for A.P), French Région Rhône-Alpes (Explo'ra Sup scholarship for C.F.M.), the Ontario Ministry of Innovation and Research, and Queen's University is acknowledged.

Notes and references

[a] *Department of Chemistry, Queen's University, Chernoff Hall, 90 Bader Lane, Kingston ON K7L3N6, Canada. Fax: (1) 613 533 6669; Tel: (1) 613 533 6587; E-mail: anne.petitjean@chem.queensu.ca*
[b] *Département de Chimie, Université d'Angers, 2 boulevard Lavoisier, 49045 Angers cedex 01, France.*
[c] *BASF, Carl-Bosch-Straße 38, 67056 Ludwigshafen, Germany.*
[d] *Department of Chemistry, University of Ottawa, 401 D'Iorio Hall, 10 Marie Curie, Ottawa K1N6N5, ON, Canada.*
[e] *Service de Spectrométrie de masse de l'Institut de Chimie de Strasbourg, 1 rue Blaise Pascal, 67000 Strasbourg, France.*

† Electronic Supplementary Information (ESI) available: synthetic details for ligands and complexes; copy of the ^{1}H and ^{13}C NMR of the ligands; ^{1}H NMR of the iron(II) complexes (1D and 2D); UV-vis titrations and Job plots for the nickel(II) and iron(II) for all ligands; details on DFT calculations, mass spectrometry, VPO and magnetism; simple models for L4-derived helicates and mesocates, loop structures and hexameric assembly; revised crystallographic data for $[Fe_2(\mathbf{L3})_3](BF_4)_4$ (CCDC# 1057879). The latter complex was already published in reference 4g, but its structure was further refined to locate all the BF_4^- anion, consistent with a 2+ oxidation state around each iron center. ^{19}F NMR analysis of the solubilized crystals also confirm that each complex is accompanied by 4 BF_4^- anions (as illustrated in ESI). See DOI: 10.1039/b000000x/

‡ ^{1}H NMR broadening may also result from intermediate exchange rates. However, it is unclear why the exchange rate would be so different in **L2a** and **L2c**.

§ The tetranuclear hexastranded complexes are represented as closed, metallomacrocyclic structures in the cartoons. Please note that there is no direct structural evidence that these are not open-stranded oligomers at this stage. However, the consistent observation of a BF_4^- only peak seems

to suggest that each iron center is coordinated to pyridyl-triazol chelates only, which can only correspond to a cyclic architecture.

¶ Elemental analysis of the powder obtained by mixing **L3M** or **L4M** and $[Fe(H_2O)_6](BF_4)_2$ or $[Ni(H_2O)_6](BF_4)_2$ in a 3:2 ratio and washing excess ligand confirmed the formation of species consistent with the $[M_2(\mathbf{LM})_3](BF_4)_4$ formula (M = Fe^{2+}, Ni^{2+}).

‖ As discussed earlier in this manuscript and apparent from Fig. 3, iron(II) complexes derived from **L2a**, **L4** and **L5** are composed of mixtures in solution. It was also not possible to obtain single crystals from these complexes. As a result, they were judged not pure enough to be submitted to magnetism studies by SQUID.

Because of intermediate exchange rate often observed for zinc complexes involving the loop ligand as well as the low solubility of the copper(I) complexes in acetonitrile, mixtures were only analyzed by ESI mass-spectrometry.

╣ isotopic patterns proved very useful to determine not only the charge of the ion for each peak, but also toconfirm the chemical nature of the ion (distinct Zn *vs* Cu patterns) as well as nuclearity (distinct pattern for a mono-nuclear and di-nuclear complexes).

1 (a) H. C. Kolb, M. G. Finn, M. G., K. B. Sharpless, *Angew. Chem. Int.* 2001, **40**, 2004; (b) H.-F. Chow, H.-F., K.-N. Lau, Z. Ke, Y. Liang, C.-M. Lo, *Chem. Commun*. 2010, **46**, 3437; (c) Y. Hua, A. H. Flood, *Chem. Soc. Rev*. 2010, **39**, 1262.

2 (a) R. M. Meudtner, S. Hecht, *Angew. Chem., Int. Ed*. 2008, **47**, 4926; (b) H. Juwarker, J. M. Lenhardt, J. C. Castillo, E. Zhao, S. Krishnamurthy, R. M. Jamiolkowski, K.-H. Kim, S. L. Craig, *J. Org. Chem*. 2009, ***74***, 8924; (d) Y. Hua, A. H. Flood, *J. Am. Chem. Soc*. 2010, **132**, 12838.

3 (a) H. Struthers, T. L. Mindt, R. Schibli, *Dalton Trans*. 2010, **39**, 675; (b) D. Schweinfurth, R. Pattacinin, S. Strobel, B. Sarkar, *Dalton Trans*. 2009, 9291; (c) D. Urankar, B. Pinter, A. Pevec, F. De Proft,I. Turel, J. Košmrlj, *Inorg. Chem*. 2010, **49**, 4820; (d) A. M. Najar, I. S. Tidmarsh, M. D. Ward, *CrystEngComm* 2010, **12**, 3642; (e) J. D. Crowley, D. A. McMorran, *Top. Heterocycl. Chem*. 2012, **28**, 31.

4 (a) J. D. Crowley, P. H. Bandeen, *Dalton Trans*. 2010, **39**, 612; (b) O. Fleischel, N. Wu, A. Petitjean, *Chem. Commun*. 2010, **46**, 8454; (c) S. O. Scott, E. L. Gavey, S. J. Lind, K. C. Gordon, J. D. Crowley, *Dalton Trans*. 2011, **40**, 12117; (d) J. T. Fletcher, B. J. Bumgarner, N. D. Engels, D. A. Skoglund, *Organometallics* 2008, **27**, 5430; (e) B. Happ, D. Escudero, M. D. Hager, C. Friebe, A. Winter, H. Görls,E. Altuntas, L. González, U. S. Schubert, *J. Org. Chem*. 2010, **75**, 4025; (f) G. Aromí, L. A. Barrios, O. Roubeau, P. Gamez, *Coord. Chem. Rev*. 2011, **255**, 485; (g) K. A. Stevenson, C. F. C. Melan, O. Fleischel, R. Wang, A. Petitjean, *Cryst. Growth Des.* 2012, **12**,5169; (h) U. R. Pokharel, F. R. Fronczek, A. W. Maverick, *Dalton Trans*. 2013, **42**, 14064.

5 (a) C. Piguet, G. Bernardinelli, G. Hopfgartner, *Chem. Rev*. 1997, **97**, 2005; (b) M. Albrecht, *Chem. Eur. J*. 2000, **6**, 3486; (c) M. Albrecht, *Chem. Rev*. 2001, **101**, 3457; (d) M. J. Hannon, L. J. Childs, *Supramol. Chem*. 2004, **16**, 7; (e) M. Albrecht, R. Froehlich, *Bull. Chem. Soc. Jpn.* 2007, **80**, 797.

6 (a) S. K. Vellas, J. E. M. Lewis, M. Shankar, A. Sagatova, J. D. A. Tyndall, B. C. Monk, C. M. Fitchett, L. R. Hanton, J. D. Crowley, Molecules 2013, **18**, 6383; (b) S. V. Kumar, W. K. C. Lo, H. J. L. Brooks, J. D. Crowley, *Inorg. Chim. Acta* 2015, **425**, 1; (c) B. Akhuli, L. Cera, B. Jana, S. Saha, C. A. Schalley, P. Ghosh, *Inorg. Chem*. 2015, **54**, 4231.

7 (a) M. M. Safont-Sempere, G. Fernández, F. Würthner, *Chem. Rev*. 2011, **111**, 5784; (b) M. L. Saha, M. Schmittel, *Org. Biomol. Chem*. 2012, **10**, 4651.

8 (a) S. Huang, R. J. Clark and L. Zhu, *Org. Lett*. 2007, **9**, 4999; (b) X.-M. Chen, R.-Q. Wang and X.-L. Yu, *Acta Cryst*. 1995, **C51**, 1545; (c) J. Breu, H. Domel and A. Stoll, *Eur. J. Inorg. Chem*. 2000, 2401.

9 (a) M. Albretch, S. Kotila, *Angew. Chem. Int. Ed. Engl*. 1995, **34**, 2134; (b) N. Ousaka, Y. Takeyama, E. Yashima, *Chem. Sci*. 2012, **3**, 466; (c) J. Xu, T. N. Parac, K. N. Raymond, *Angew. Chem. Int. Ed. Engl*. 1999, **38**, 2878.

10 B. R. Serr, K. A. Andersen, C. M. Elliott, O. P. Anderson, *Inorg. Chem*. 1988, **27**, 4499.

11 (a) E. T. Adams, P. J. Jr. Wan, E. F. Crawford, *Methods Enzymol*. 1978, **48**, 69; (b) E. T. Jr. Adams, *J. Lipid Res*. 1986, **27**, 1233.

12 D. Alagille, R. M. Baldwin, B. L. Roth, J. T. Wroblewski, E. Grajkowska , G. D. Tamagnan, *Bioorg. Med. Chem.* 2005, **13**, 197.

13 (a) "Spin Crossover in Transition Metal Compounds I', P. Gütlich, H. A. Goodwin, *Topics in Current Chemistry*, Springer-Verlag Berlin Heidelberg 2004, Chapt. 3; (b) D. Onggo, J. M. Hook, A. D. Rae and H. A. Goodwin, *Inorg. Chim. Acta*, 1990, **173**, 19; (c) L. J. Charbonnière, A. F. Williams, C. Piguet, G. Bernardinelli and E. Rivara-Minten, *Chem. Eur. J*., 1998, **4**, 485; (d) F. Tuna, M. R. lees, G. J, Clarkson, M. J. Hannon, *Chem. Eur. J*. 2004, **10**, 5737; (e) M. H. Klingele, B. Moubaraki, J. D. Cashion, K. S. Murray, S. Brooker, *Chem. Commun*. 2005, 987; (f) Y. Garcia, C. M. Grunert, S. Reiman, O. van Campenhoudt, P. Gütlich, *Eur. J. Inorg. Chem.* 2006, 3333; (g) D. Pelleteret, R. Clérac, C. Mathonière, E. Harté, W. Schmitt, P. E. Kruger, *Chem. Commun*. 2009, 221; (h) Y. Sunatsuki, R. Kawamoto, K. Fujita, H. Maruyama, T. Suzuki, H. Ishida, M. Kojima, S. Iijima, N. Matsumoto, *Inorg. Chem*. 2009, **48**, 8784; (i) J. J. M. Amoore, C. J. Kepert, J. D. Cashion, B. Moubaraki, S. M. Neville, K. S. Murray, *Chem. Eur. J*. 2006, **12**, 8220; (j) J. J. M. Amoore, S. M. Neville, B. Moubaraki, S. S. Iremonger, K. S. Murray, J.-F. Létard, C. J. Kepert, *Chem. Eur. J*. 2010, **16**, 1973; (k) R. J. Archer, C. S. Hawes, G. N. L. Jameson, V. McKee, B. Moubaraki, N. F. Chilton, K. S. Murray, W. Schmitt, P. E. Kruger, *Dalton Trans*. 2011, **40**, 12368; (l) N. Chandrasekhar, R. Chandrasekar, *Dalton Trans*. 2010, **39**, 987; (m) C. Cook, F. Habib, T. Aharen, R. Clérac, A. Hu, M. Murugesu, *Inorg. Chem*. 2013, **52**, 1825.

14 For examples of cell-related self-sorting, see (a) D. Voet, J. D. Voet, *Biochemistry*, Wiley, New York, 2011, Chapters on nucleic acids (29) and on viruses (33), and an interesting commentary in (b) S. Ventegodt, T. D. Hermansen, T. Flensbord-Madsen, M. L. Nielsen, B. Clausen, J. Merrick, *The Scientific World Journal* 2006, **6**, 1132. For an example on the self-organization of cells into tissues (review in neurology), see (c) M. Karus, S. Blaess, O. Brüstle, *J. Comp. Neurol*. 2014, **522**, 2831. (d) R. Krämer, J.-M. Lehn, A. Marquis-Rigault, *Proc. Natl. Acad. Sci. USA* 1993, **90**, 5394.